Copper-Doped ZnS with Internal Phase Junctions for Highly Selective CO Production from CO_2 Photoreduction

Xiandi Zhang,[1,2,†] *Daekyu Kim,*[2,†] *and Lawrence Yoon Suk Lee*[1,2,3,*]

[1] The Hong Kong Polytechnic Shenzhen Research Institute, Nanshan, Shenzhen, China

[2] Department of Applied Biology and Chemical Technology and the State Key Laboratory of Chemical Biology and Drug Discovery, The Hong Kong Polytechnic University, Hung Hom, Kowloon, Hong Kong SAR, China

[3] Research Institute for Smart Energy, The Hong Kong Polytechnic University, Hung Hom, Kowloon, Hong Kong SAR, China

[†] These authors equally contributed to this work.

*E-mail: lawrence.ys.lee@polyu.edu.hk (L. Y. S. Lee)

Keywords: CO_2 reduction reaction; photocatalysis; multiple phase junction; Cu doping; zinc sulfide

Abstract

ZnS is one of the promising earth-abundant catalysts for photoreduction reactions. The performance of ZnS on CO_2 reduction is, however, limited by its wide bandgap, fast recombination of charge carriers, as well as low product selectivity due to the competing hydrogen evolution reaction (HER). Herein, a Cu-doped ZnS containing abundant sphalerite and wurtzite phase (S–W) junctions is prepared and an enhanced photocatalytic activity with a high selectivity on CO production is demonstrated. Both experimental and theoretical results reveal that Cu incorporation and S–W phase junction enhance light absorption and promote photocatalytic activity. The presence of Cu ion contributes to the CO generation and suppress the competing HER by enhancing the bonding of catalyst surface with •CO adsorbates. This work provides useful insights into the modification of CO_2 reduction photocatalysts to realize high catalytic efficiency and product selectivity.

KEYWORDS: internal phase junction, copper ion doping, photocatalysis, CO_2 conversion, CO selectivity

Introduction

The rapid increase in energy consumption over the past decades has raised global concerns about the depletion of fossil fuels, and as a consequence, the level of atmospheric carbon dioxide (CO_2) has reached the highest in history.{Christoforidis, 2018 #9;Li, 2018 #30} A promising approach to address these issues simultaneously is to convert CO_2 into fuels and value-added chemicals by using clean and renewable solar energy.{White, 2015 #10;Shehzad, 2018 #31} Despite the vast effort devoted to the developing of photocatalysts for effective CO_2 reduction, the conversion rates of most photocatalysts are still limited by the fast recombination of photogenerated charge carriers. The low selectivity on the target product due to the complex nature of CO_2 reduction reaction (CRR) is another hurdle to overcome.{Li, 2019 #11;Habisreutinger, 2013 #33} For practical application of photocatalytic CRR system, new strategies for enhancing the intrinsic activity of photocatalyst need to be explored with the surface design for product selectivity.

ZnS, an important II-VI group transition metal sulfide, is one of the most studied semiconductors for photocatalysis.{Guzman, 2010 #48;Zhou, 2016 #50;Zhou, 2014 #51} It has a wide bandgap (3.6 ~ 3.8 eV) and a relatively negative reduction potential of *ca*. −1.8 V (*vs*. standard hydrogen electrode, SHE), which is particularly suitable for photocatalytic reduction reactions, including hydrogen evolution reaction from water,{Zhang, 2013 #16} prebiotic synthesis,{Zhang, 2007 #49} CO_2 reduction,{Chen, 2013 #8} dye degradation,{Chauhan, 2014 #15} and coenzyme regeneration.{Dibenedetto, 2012 #13} Despite its appropriate band position and high theoretical efficiency for photocarrier generation, the performances of ZnS in photocatalytic applications are restricted by the fast recombination of charge carriers and low utilization efficiency of solar light (*ca*. 5 % of solar spectrum).{Fang, 2015 #17} Various methods have been developed for enhancing the performance of ZnS in photocatalytic reactions, for instance, defects engineering{Hao, 2018 #18} and selective exposure of facets.{Liu, 2013 #19} Recently, the internal interface between two distinct crystal structures of semiconductor, so-called homojunction, has been explored as an active catalytic site.{Fang, 2015 #17;Liu, 2013 #20} Such internal interfaces are known to effectively prevent the recombination of photogenerated electron–hole pairs. In the case of ZnS, the construction

of multiple parallel phase junctions between sphalerite and wurtzite phases has been reported to dramatically promote the hydrogen evolution rate owing to easier H^+ adsorption and enhanced H_2 desorption at the interface.{Liu, 2018 #1}

Elemental doping offers a versatile way to tune surface properties, such as surface electronic structure, to enhance CO_2 adsorption and thus improve the interaction with CO_2.{Guo, 2017 #5;Chen, 2013 #8;Chen, 2013 #8;Baran, 2015 #2} Dopants in an appropriate amount can enhance light absorption and act as an active site that prevents the recombination of charge carriers by trapping electrons and holes.{Lee, 2016 #21} Various elements, including Au,{Zhang, 2013 #16} Ru,{Baran, 2015 #2} and Ni,{Chen, 2013 #8} have been engaged as dopants for semiconductor-based CRR catalysts to demonstrate such promotional effects. Particularly, Cu species of different oxidation states have shown a specific product selectivity in addition to the enhanced light absorption.{Nasution, 2005 #6;Pham, 2017 #7}

Herein, we report the design and preparation of Cu-doped ZnS nanocrystals that contain abundant internal interfaces between sphalerite and wurtzite phases. The two-step synthetic approach, which involves the ZnS-ethylenediamine complex ($Zn(en)_{0.5}S$) as an intermediate, allows the simultaneous incorporation of Cu ions and creation of phase junctions in ZnS to enhance CO production rate as well as the CO selectivity from photocatalytic CRR. The synergistic effect of Cu doping and internal phase junction on photocatalytic CRR efficiency would be discussed based on the results from both experiments and calculations.

Experimental section

Materials and chemicals

Zinc acetate ($Zn(OAc)_2$, 99.99 %), copper (II) acetate ($Cu(OAc)_2$, 99.99 %), ethylenediamine (en, 99 %), L-cystine (98 %), Nafion® 117 solution (5 wt.%), chloroform (99.8 %), 2-proponal (99.9 %), and ethanol (96 %) were purchased from Sigma–Aldrich. All chemicals and solvents were used without further purification.

Synthesis of ZnS, and Cu-ZnS

$ZnS(en)_{0.5}$ was first prepared as the precursor for ZnS synthesis.{Fang, 2015 #17} Briefly, $Zn(OAc)_2$ (2 mmol) and L-cysteine (4 mmol) were dissolved in ethylenediamine (30 mL) under magnetic stirring. The solution was then transferred to a 50 mL Teflon-lined stainless-steel

autoclave and heated to 180 °C for 24 h. After cooling to room temperature, $ZnS(en)_{0.5}$ precursor was collected by centrifugation, washed with deionized water and ethanol three times, and dried in a vacuum oven at 50 °C. The dried $ZnS(en)_{0.5}$ precursor (50 mg) was dispersed in deionized (DI) water (30 mL) and hydrothermally treated at 180 °C for 12 h. The final product was obtained by centrifugation, followed by washing with ethanol and water and drying in a vacuum oven at room temperature overnight. Cu-doped ZnS was synthesized using a similar procedure with the addition of $Cu(OAc)_2$ (0.1, 0.2, 0.3, and 0.4 mmol) during the preparation of precursor, and the obtained samples were named after the mol.% of $Cu(OAc)_2$ as $Cu_{0.05}$-ZnS, $Cu_{0.1}$-ZnS, $Cu_{0.15}$-ZnS, and $Cu_{0.2}$-ZnS, respectively.

Synthesis of Sphalerite–Wurtzite ZnS (SW-ZnS)

The synthetic procedure of ZnS containing sphalerite–wurtzite mixed phase (SW-ZnS) was similar to that of ZnS, except for the hydrothermal reaction temperature. $Zn(en)_2$ (50 mg) was dispersed in DI water (30 mL) and hydrothermally treated at 220 °C for 12 h. Upon cooling down, the product was collected by centrifugation, followed by washing with ethanol and water, and dried in a vacuum oven at room temperature overnight.

Materials Characterization

Powder X-ray diffraction (XRD) patterns were recorded on a Rigaku SmartLab 9kW X-ray Diffractometer at a scan rate of 3° min^{-1}. Transmission electron microscopic (TEM) images and high-resolution TEM (HRTEM) images were obtained using a JEOL Model JEM-2100F operated with a field emission gun at 200 kV. UV–vis diffuse reflectance spectra (UV–vis DRS) were measured using a Cary 4000 UV–vis spectrophotometer from 200 to 800 nm wavelength. X-ray photoelectron spectroscopy (XPS) was carried out using an ESCALAB 250Xi X-ray photoelectron spectrometer (Thermo Fisher) with a 12 kV Al Kα radiation source. XPS data were treated with CasaXPS software using a background type of Shirley and peak profile of Gaussian–Lorentzian GL(30). Electron spin resonance (ESR) spectroscopy was conducted using an ANANI SPINSCAN X spectrometer at room temperature.

Photocatalytic CO_2 reduction reaction

Photocatalytic CO_2 reduction reaction was carried out in a closed system using a Pyrex reaction cell (50 mL). First, the as-prepared catalyst (5 mg) was dispersed in a solution containing

chloroform (18 mL) and 2-propanol (2 mL) and degassed with high-purity CO_2 for 30 min. The solution was then irradiated with a Xenon lamp (Ceaulight, 300 W, 1 sun). The distance from the lamp to the center of the photoreactor was fixed at 20 cm, and the average light intensity irradiated on the photoreactor was *ca.*100 mW cm^{-2}. Gaseous products were analyzed using a gas chromatograph system (Agilent 7890 B) equipped with a thermal conductivity detector (TCD) and a flame ionization detector (FID). Liquid products were detected by ^1H nuclear magnetic resonance spectroscopy (NMR, Bruker Advance-III). For the stability test, five consecutive 2-hour reactions were carried out under the same conditions. The reaction cell was purged with CO_2 for 30 min before each run without adding more catalysts.

Computational calculations

Density function theory (DFT) calculations were performed using the CP2K package.{Hutter, 2014 #36} The system was described by the PBE functional{Perdew, 1996 #37} with Grimme D3 correction.{Grimme, 2006 #38} Kohn–Sham DFT was employed as the electronic structure method in the framework of Gaussian and plane waves method.{VandeVondele, 2007 #39;VandeVondele, 2005 #40} The molecules were described by the Goedecker–Teter–Hutter (GTH) pseudopotentials{Goedecker, 1996 #41;Hartwigsen, 1998 #42} and DZVP–MOLOPT–GTH basis sets.{VandeVondele, 2007 #39} The electronic structure analysis was carried out in terms of the projected density of state (PDOS). In the calculations, the wurtzite phase was modeled with a 4 × 4 × 3 super-cell in a 15.515 × 15.515 × 18.7821 hexagonal box and the sphalerite phase was modeled with a 3 × 3 super-cell in a 16.400 cubic box. The sphalerite–wurtzite mixed phase was modeled with a 15.515 × 15.515 × 24.6428 box where top of four layers was associated to wurtzite phase while the bottom layers were sphalerite phase.

Result and Discussion

Synthesis of Sphalerite-Wurtzite Cu-ZnS

Cu-doped ZnS nanocrystals were prepared in a two-step solvothermal/hydrothermal reaction in which zinc and copper salts ($Zn(OAc)_2$ and $Cu(OAc)_2$) were reacted with L-cysteine, which was both a capping ligand and a sulfur source, in ethylenediamine (for details, see Experimental Section). Based on the mol.% of $Cu(OAc)_2$ used, the final products were named $Cu_{0.05}$-ZnS and $Cu_{0.1}$-ZnS. For comparison, pristine ZnS was also prepared using a similar method but in

the absence of $Cu(OAc)_2$.

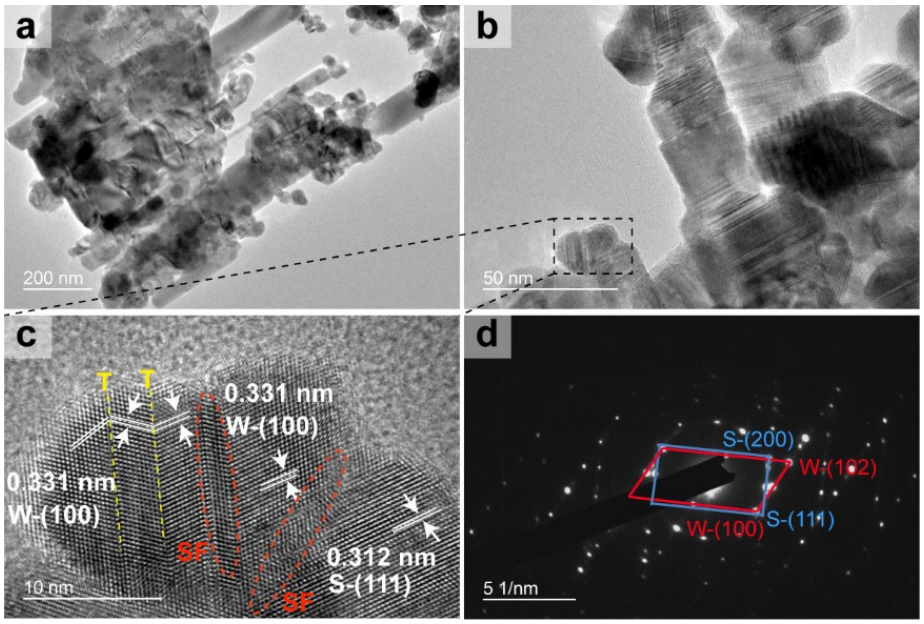

Figure 1. (a, b) TEM, (c) HRTEM images, and (d) SAED pattern of $Cu_{0.1}$-ZnS.

The transmission electron microscopic (TEM) images of all three samples show irregular shapes of plate-like morphology (**Figures 1a**, **S1a**, and **S1c**). A closer examination of the $Cu_{0.1}$-ZnS nanoplates reveals their rough surface displaying multiple parallel stripes (**Figure 1b**). The high-resolution TEM (HRTEM) image in **Figure 1c** shows typical stacking faults (SF, red circles) and twin boundaries (T, yellow lines). Interestingly, two distinct lattice fringes of d = 0.331 and 0.312 nm are observable, which correspond to the (100) facet of hexagonal wurtzite ZnS and the (111) facet of cubic sphalerite ZnS, respectively.{Fang, 2015 #17} The coexistence of the two phases is also supported by the two sets of diffraction spots in the selected area electron diffraction (SAED) pattern shown in **Figure 1d**. Similar surface features of stacking faults and twin boundaries are observed in $Cu_{0.05}$-ZnS and ZnS (**Figures S1b** and **S1d**). Both wurtzite and sphalerite phases are identified in the HRTEM image of $Cu_{0.05}$-ZnS, whereas only the wurtzite phase is visible from ZnS. Elemental mapping images in **Figure S2** show Zn, Cu, and S elements homogeneously distributed in $Cu_{0.1}$-ZnS. Energy dispersive spectroscopic (EDS) data verify that $Cu_{0.05}$-ZnS and $Cu_{0.1}$-ZnS contain 7.28 and 11.60 at.% Cu, respectively (**Table S1**).

Powder X-ray diffraction (XRD) spectroscopy was used to investigate the crystal structure of samples (**Figure 2a**). Pristine ZnS exhibits a diffraction pattern of hexagonal wurtzite phase

ZnS (JCPDS # 36-1450) with the characteristic peaks at 26.9°, 28.8°, 30.5°, 39.6°, 47.6°, 51.8°, 55.5°, 56.4°, 72.9°, and 77.8°, which are assigned to the (100), (002), (101), (102), (110), (103), (200), (112), (203), and (211) planes, respectively. The Cu-ZnS samples display XRD patterns similar to those of ZnS, however, the peak at 28.6° is much more intensified, especially for $Cu_{0.1}$-ZnS. Moreover, three new peaks at 32.9°, 69.2°, and 79.8° are observed from both Cu-ZnS samples, which correspond to the (200), (400), and (311) planes of cubic sphalerite ZnS phase (JCPDS #05-0566), respectively, confirming the coexistence of wurtzite and sphalerite phases in the Cu-ZnS samples. It is worth noting that the diffraction peaks in the Cu-ZnS samples show an obvious positive shift of 0.3°. This shift is caused by the insertion of Cu atoms that have a smaller radius (0.57 Å) than Zn atoms (0.60 Å),{Lee, 2016 #21;Ummartyotin, 2012 #22} indicating the successful incorporation of Cu in ZnS sphalerite–wurtzite (S–W) crystal phase. Further increase of Cu doping level to 15 and 20 wt.% ($Cu_{0.15}$-ZnS and $Cu_{0.2}$-ZnS, respectively) resulted in forming a $Cu_{1.96}S$ phase (JCPDS #12-0174) as indicated by diffraction peaks at 26.9, 31.3, 44.9, and 53.2° in **Figure S3**. This suggests that the highest Cu doping level that preserves the original ZnS crystal structure is 10 wt.%.

The composition and structure of the Cu-ZnS samples are well supported by X-ray photoelectron spectroscopy (XPS) data. The XPS survey spectra of both Cu-ZnS samples identify the peaks in the C 1s, Zn 2p, Cu 2p, and S 2p regions, while the peaks in the Cu 2p region are absent from pristine ZnS (**Figure S4**). **Figure 2b** compares the high-resolution XPS spectra of ZnS and $Cu_{0.1}$-ZnS in the Zn 2p region. The pristine ZnS exhibits a typical pair of peaks at 1,021.98 and 1,045.05 eV, corresponding to $2p_{3/2}$ and $2p_{1/2}$ states of Zn^{2+} species, respectively.{Jiaguo Yu, 2010 #23;Li, 2014 #24} These peaks in $Cu_{0.1}$-ZnS are positively shifted to 1,022.52 and 1,045.47 eV, respectively, indicating the electron redistribution in Zn atoms due to Cu incorporation.{Lee, 2016 #21} Similar yet opposite peak shifts are seen in the S 2p region (**Figure 2c**). The S $2p_{3/2}$ and $2p_{1/2}$ peaks of $Cu_{0.1}$-ZnS are shifted to 161.33 and 162.51 eV compared with 161.57 and 162.79 eV of ZnS, respectively, balancing the electron distribution in $Cu_{0.1}$-ZnS.{Ul Abideen, 2018 #26} In the high-resolution Cu 2p XPS spectrum, two symmetric peaks are observed at 933.02 and 952.81 eV, which is a clear evidence of Cu doping and suggests that Cu^{2+} is the major species[30] (**Figure 2d**).

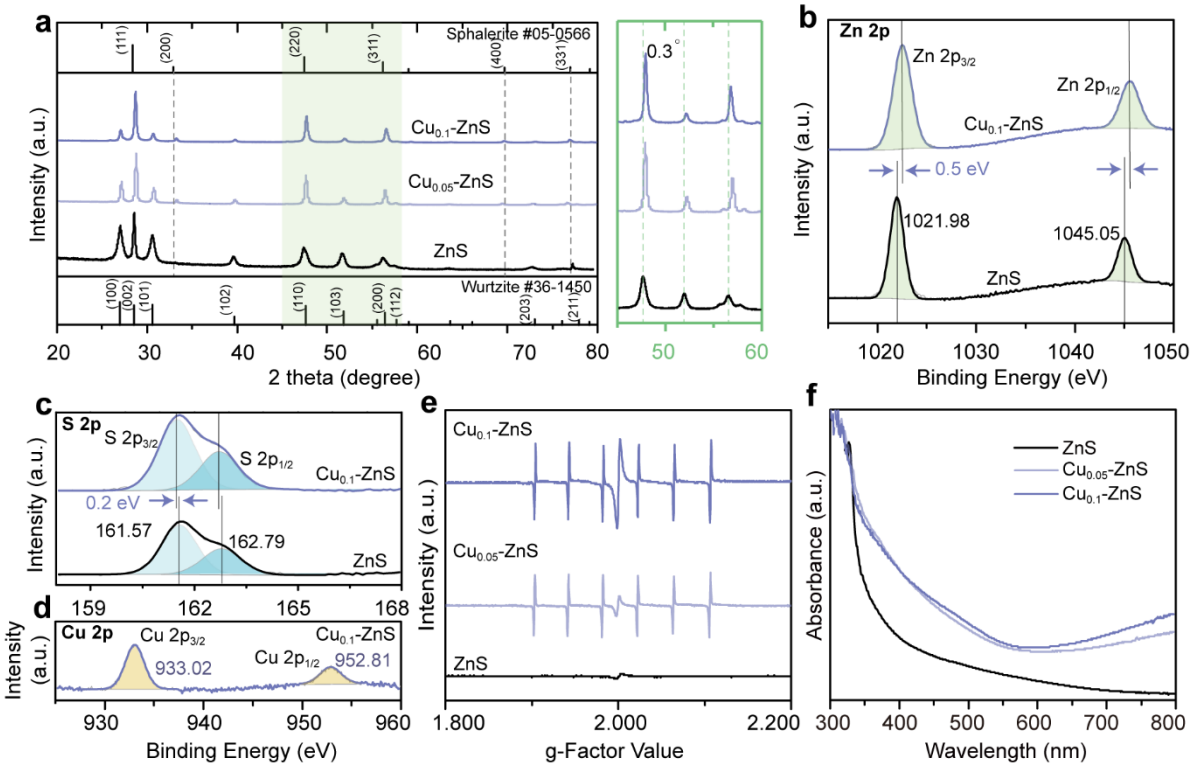

Figure 2. (a) XRD patterns of ZnS, $Cu_{0.05}$-ZnS, and $Cu_{0.1}$-ZnS. High-resolution XPS spectra of ZnS and $Cu_{0.1}$-ZnS in (b) Zn 2p, (c) S 2p, and (d) Cu 2p regions. (e) ESR and (f) UV-Vis DRS spectra of ZnS, $Cu_{0.05}$-ZnS, and $Cu_{0.1}$-ZnS.

Electron spin resonance (ESR) spectroscopy was employed to verify the existence of defect sites indicated by TEM analysis of $Cu_{0.1}$-ZnS, and the results are presented in **Figure 2e**. Both Cu-ZnS samples clearly show six sharp peaks located at the g-factor values of 1.911, 1.941, 1.982, 2.022, 2.064, and 2.106, which are the characteristics of the sphalerite phase ZnS.{Fang, 2015 #17} In contrast, pristine ZnS displays no such sharp peaks, confirming its pure wurtzite phase. Another ESR signal at 2.001 is evident in all samples, which, agreeing well with the TEM observations, can be attributed to the defect species of stacking faults and twin crystals (**Figure 1**).{Fang, 2015 #17} Because the intensity of ESR signal is directly related to the density of defects,{Godefroo, 2008 #27} $Cu_{0.01}$-ZnS, with the most intense peak at 2.001, contains the highest density of defects, while pristine ZnS has only trace amounts of defect sites. The relationship among Cu doping, S–W phase junctions, and defects could be understood by considering the synthetic conditions. A ZnS nanocrystal was prepared in a two-step reaction that involves ethylenediamine-intercalated ZnS precursor ($Zn(en)_{0.5}S$). The high surface energy of $Zn(en)_{0.5}S$ under hydrothermal conditions drives its surface atomic

rearrangements, rendering the stacking faults and twin boundaries on the surface of the resultant ZnS.{Fang, 2015 #17;Liu, 2018 #1} The incorporation of Cu atoms disturbs the atomic arrangement of $Zn(en)_{0.5}S$, making the surface more unstable, which eventually induces more defective sites or even partial phase transformation to form the S–W junctions in Cu-ZnS.{Lee, 2016 #21}

The optical properties of ZnS and Cu-ZnS are studied using UV–vis diffraction reflectance spectroscopy (UV–vis DRS) to investigate the influence of metal doping and defect sites on the band structure (**Figure 2f**). Pristine ZnS exhibits a typical absorption edge at 370 nm in the UV region with the corresponding bandgap energy (E_g) of 3.64 eV (**Figure S5**).{Liu, 2018 #1;Baran, 2015 #2} Upon the incorporation of Cu, the absorption edges of Cu-ZnS shift to a longer wavelength and the bandgap is decreased to 3.37 eV (**Figure S5**). Such a red-shift of absorption band was reported to arise from Cu^{2+} doping or S–W junctions.{Liu, 2018 #1;Patel, 2016 #3} In addition, both Cu-ZnS samples display an absorption tail in the visible-light region (600–800 nm), which can be visualized with an apparent color change from white to brown (insets in **Figure S5**). It has been suggested that the CuS domains formed by preferential Cu^{2+} doping could exert a strong localized surface plasmon resonance effect,{Arai, 2008 #4} leading to the enhanced light absorption at wavelengths over 600 nm.

Photocatalytic CO_2 Reduction Reaction Performance

The photocatalytic activities of ZnS and Cu-ZnS toward CO_2 reduction reaction (CRR) were compared to understand the effect of Cu ion doping and S–W phase junction, as well as the altered optical property. The reduction products were analyzed by gas chromatography and ^1H NMR and the results are summarized in **Figure 3a**. Both ZnS and Cu-ZnS samples mainly produce CO and H_2 and no liquid products are detected. Pristine ZnS shows a CO production rate of 39.7 μmol g^{-1} h^{-1} with 95.0 % of CO selectivity. As the only side product, H_2 is generated with a production rate of 2.1 μmol g^{-1} h^{-1}. Both CO production rate and CO selectivity are enhanced with the increase in the level of Cu doping onto the ZnS. Particularly, a high CO selectivity of 99.9 % with a production rate of 68.9 μmol g^{-1} h^{-1} is achieved with $Cu_{0.1}$-ZnS. The competing H_2 generation is almost completely suppressed and only a trace amount of H_2 is detected. The $Cu_{0.1}$-ZnS maintains the photocatalytic CO production rate in

five consecutive 2 h-reactions with no apparent loss of activity, demonstrating its excellent stability against photocorrosion (**Figure 3b**). The XRD pattern and TEM images of $Cu_{0.1}$-ZnS collected after the catalysis confirm that its crystal structure and morphology remain unchanged. (**Figures 3c** and **S6**). Several control experiments were conducted to ensure the production of CO by photocatalytic reduction of CO_2 (**Figure 3d**).{Zhu, 2018 #28} When Ar is purged instead of CO_2 gas under the same conditions, no detectable amount of CO is produced. Other tests conducted without irradiation or catalyst show no CO production activity, verifying that CO is generated from photocatalytic CRR.

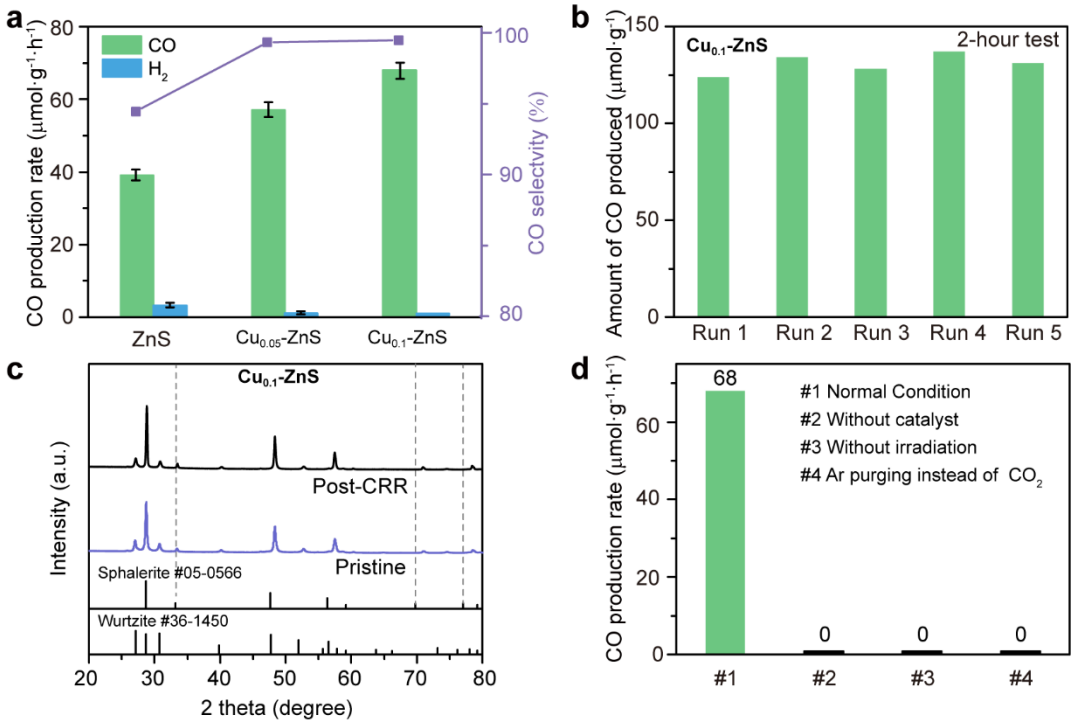

Figure 3. (a) Photocatalytic CO_2 reduction over ZnS, $Cu_{0.05}$-ZnS, and $Cu_{0.1}$-ZnS. (b) Stability test and (c) XRD patterns of $Cu_{0.1}$-ZnS before and after photocatalytic CRR. (d) Control experiments conducted with $Cu_{0.1}$-ZnS under various conditions.

Effect of phase junction and Cu doping on CO_2 reduction

The incorporations of Cu ion and S–W phase junction in ZnS apparently promoted the photocatalytic activity and CO selectivity of Cu-ZnS samples. The S–W phase junction was reported to contain abundant sulfur vacancies,[12] which is also supported by the ESR result (**Figure 2e**). It was previously reported that vacant sites near the phase junction could effectively facilitate the separation of charge carriers and localization of photoelectrons for surface catalysis, thus promote the photocatalytic performance.{Liu, 2018 #1;Fang, 2015 #17}

However, it has never been reported how the internal S–W phase junctions affect the CRR process in terms of product selectivity. To clarify the role of Cu doping and S–W phase junctions in photocatalytic CRR, a control sample of ZnS containing S–W mixed phase (SW-ZnS) was prepared following the procedure of a previous report[16] (for details, see Experimental Section). Both sphalerite and wurtzite peaks are evident in the XRD pattern of SW-ZnS (**Figure 4a**) and the ESR spectrum of SW-ZnS suggests the co-existence of mixed phase and comparable density of defects to Cu-ZnS (**Figure S7c**). In the photocatalytic CRR test, SW-ZnS achieves the CO and H_2 production rates of 57.9 and 16.0 μmol g^{-1} h^{-1}, respectively, showing an overall improvement in photocatalytic activity by S–W phase junctions (**Figure 4b**). The CO selectivity of SW-ZnS, however, decreases to 78.4 % from 95.0 % of ZnS, indicating that the formation of S–W phase junction is more favorable for HER than for CRR.

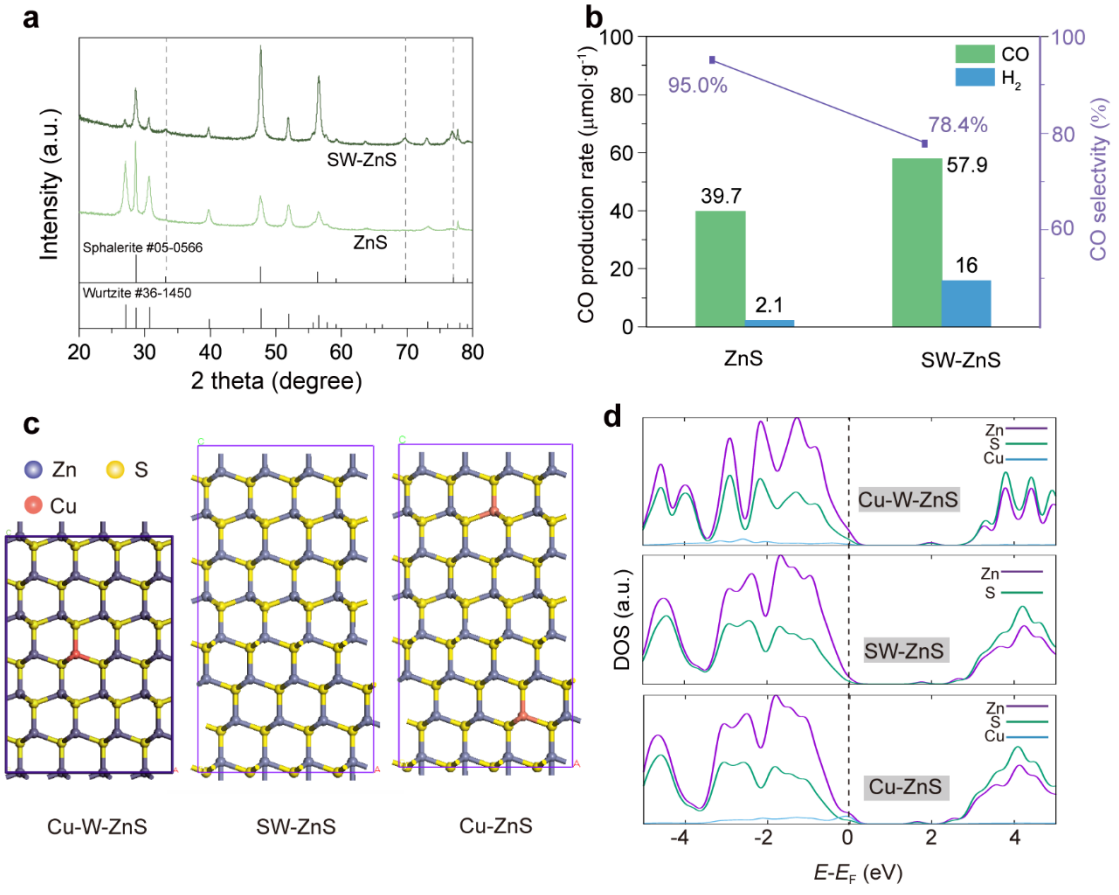

Figure 4. (a) XRD patterns and (b) photocatalytic CO_2 reduction rates and CO selectivity of SW-ZnS and ZnS. (c) Most stable atomic configurations at the surface of Cu-W-ZnS, SW-ZnS, and Cu-ZnS. Zn, S, and Cu atoms are represented by purple, yellow, and red balls, respectively. (d) PDOS of Cu-W-ZnS, SW-ZnS, and Cu-ZnS.

Cu ion doping is believed to play an important role in the tuning of surface property to

favor CO production. To further elucidate the role of Cu ion in the enhancement of photocatalytic activity and CO selectivity, density functional theory (DFT) calculations were carried out. Three models, Cu-doped ZnS (Cu-W-ZnS), sphalerite–wurtzite mixed ZnS (SW-ZnS), and Cu-doped mixed-phased ZnS (Cu-ZnS), are developed as illustrated in **Figure 4c** and the corresponding projected density of states (PDOS) are shown in **Figure 4d**. Among the three types of ZnS, the calculated bandgap of Cu-ZnS, consistent with the experimental results, is the smallest. Comparison of the PDOS plots between SW-ZnS and Cu-ZnS clearly shows that the incorporation of Cu contributes to the electron density at the Fermi level, suggesting a promoted reactivity on the Cu site (**Figure 4d**, middle and bottom).{Lin, 2019 #34} Meanwhile, such promotional effect on the electron density at the Fermi level also enhances the bonding of catalyst surface with absorbates, •CO intermediate in this case, thus leading to an increased CO selectivity with Cu doping.{Hammer, 1996 #35} However, without S–W internal phase, this contribution to the Fermi level from Cu atoms is much weaker in the Cu-doped pure wurtzite phase (**Figure 4d**, top), indicating the synergistic effect of the introduction of Cu and S–W internal phase junction.

Conclusion

In summary, ZnS nanocrystals with homogenous Cu-doping and abundant internal S–W phase junctions were prepared as a CO_2 reduction photocatalyst. The formation of internal phase junction is closely related to Cu-doping and can be regulated by controlling the Cu doping level. Compared with pristine ZnS, $Cu_{0.1}$-ZnS shows enhanced photocatalytic CO_2 reduction reaction rate and CO selectivity. Both Cu doping and S–W phase junction promote light absorption and thus contribute to photocatalytic activity. The highly improved CO selectivity of $Cu_{0.1}$-ZnS is due to the doped Cu ions that increase the bonding between catalyst surface and CO intermediate according to the DFT calculations. This work provides an effective strategy for tailoring the property of metal sulfides to realize enhanced CO_2 reduction reaction with high product selectivity.

Acknowledgements

X. Zhang and D. Kim equally contributed to this work. We gratefully acknowledge the financial supports from the Shenzhen Science, Technology, and Innovation Commission (SZTIC, Grant No. JCYJ20170818105046904) and The Hong Kong Polytechnic University (1-BE0Y).

Supporting Information

Supporting Information, including TEM, XPS, post-HER XRD, and DFT calculation, is available from online version.

Conflict of Interest

The authors declare no conflict of interest.

Reference

(1) Christoforidis, K. C.; Fornasiero, P. Photocatalysis for Hydrogen Production and CO_2 Reduction: The Case of Copper-Catalysts. *ChemCatChem* **2018,** *11*, 368-382.

(2) Li, R.; Zhang, W.; Zhou, K. Metal-Organic-Framework-Based Catalysts for Photoreduction of CO_2. *Adv. Mater.* **2018,** *30*, 1705512.

(3) White, J. L.; Baruch, M. F.; Pander Iii, J. E.; Hu, Y.; Fortmeyer, I. C.; Park, J. E.; Zhang, T.; Liao, K.; Gu, J.; Yan, Y.; Shaw, T. W.; Abelev, E.; Bocarsly, A. B. Light-Driven Heterogeneous Reduction of Carbon Dioxide: Photocatalysts and Photoelectrodes. *Chem. Rev.* **2015,** *115*, 12888-12935.

(4) Shehzad, N.; Tahir, M.; Johari, K.; Murugesan, T.; Hussain, M. A Critical Review on TiO_2 Based Photocatalytic CO_2 Reduction System: Strategies to Improve Efficiency. *J. CO_2 Util.* **2018,** *26*, 98-122.

(5) Li, X.; Yu, J.; Jaroniec, M.; Chen, X. Cocatalysts for Selective Photoreduction of CO_2 into Solar Fuels. *Chem. Rev.* **2019,** *119*, 3962-4179.

(6) Habisreutinger, S. N.; Schmidt-Mende, L.; Stolarczyk, J. K. Photocatalytic Reduction of CO_2 on TiO_2 and Other Semiconductors. *Angew. Chem. Int. Ed.* **2013,** *52*, 7372-7408.

(7) Guzman, M. I.; Martin, S. T. Photo-Production of Lactate from Glyoxylate: How Minerals Can Facilitate Energy Storage in a Prebiotic World. *Chem. Commun.* **2010,** *46*, 2265-7.

(8) Zhou, R.; Guzman, M. I. Photocatalytic Reduction of Fumarate to Succinate on ZnS Mineral Surfaces. *J. Phys. Chem. C* **2016,** *120*, 7349-7357.

(9) Zhou, R.; Guzman, M. I. CO_2 Reduction under Periodic Illumination of ZnS. *J. Phys. Chem. C* **2014,** *118*, 11649-11656.

(10) Zhang, J.; Wang, Y.; Zhang, J.; Lin, Z.; Huang, F.; Yu, J. Enhanced Photocatalytic Hydrogen Production Activities of Au-Loaded ZnS Flowers. *ACS Appl. Mater. Interfaces* **2013,** *5*, 1031-1037.

(11) Zhang, X. V.; Ellery, S. P.; Friend, C. M.; Holland, H. D.; Michel, F. M.; Schoonen, M. A. A.; Martin, S. T. Photodriven Reduction and Oxidation Reactions on Colloidal Semiconductor Particles: Implications for Prebiotic Synthesis. *J. Photochem. Photobiol. A* **2007,** *185*, 301-311.

(12) Chen, J.; Xin, F.; Qin, S.; Yin, X. Photocatalytically Reducing CO_2 to Methyl Formate in Methanol over ZnS and Ni-doped ZnS Photocatalysts. *Chem. Eng. J.* **2013,** *230*, 506-512.

(13) Chauhan, R.; Kumar, A.; Pal Chaudhary, R. Photocatalytic Degradation of Methylene Blue with Cu Doped ZnS Nanoparticles. *J. Lumin.* **2014,** *145*, 6-12.

(14) Dibenedetto, A.; Stufano, P.; Macyk, W.; Baran, T.; Fragale, C.; Costa, M.; Aresta, M. Hybrid Technologies for an Enhanced Carbon Recycling Based on The Enzymatic Reduction of CO_2 to Methanol in Water: Chemical and Photochemical NADH Regeneration. *ChemSusChem* **2012,** *5*, 373-378.

(15) Fang, Z.; Weng, S.; Ye, X.; Feng, W.; Zheng, Z.; Lu, M.; Lin, S.; Fu, X.; Liu, P. Defect Engineering and Phase Junction Architecture of Wide-Bandgap ZnS for Conflicting Visible Light Activity in Photocatalytic H_2 Evolution. *ACS Appl. Mater. Interfaces* **2015,** *7*, 13915-13924.

(16) Hao, X.; Wang, Y.; Zhou, J.; Cui, Z.; Wang, Y.; Zou, Z. Zinc Vacancy-Promoted Photocatalytic Activity and Photostability of ZnS for Efficient Visible-Light-Driven Hydrogen Evolution. *Appl. Catal. B Environ.* **2018,** *221*, 302-311.

(17) Liu, S.; Wang, X.; Wang, K.; Lv, R.; Xu, Y. ZnO/ZnS–PdS Core/shell Nanorods: Synthesis, Characterization and Application for Photocatalytic Hydrogen Production from a Glycerol/Water Solution. *Appl. Surf. Sci.* **2013,** *283*, 732-739.

(18) Liu, M.; Jing, D.; Zhou, Z.; Guo, L. Twin-Induced One-Dimensional Homojunctions Yield High Quantum Efficiency for Solar Hydrogen Generation. *Nat. Commun.* **2013,** *4*, 2278-2286.

(19) Liu, W.; Ha, E.; Wang, L.; Hu, L.; Lee, L. Y. S.; Wong, K.-Y. Creating Multiple Parallel Internal Phase Junctions on ZnS Nanoparticles as Highly active catalytic sites. *Adv. Mater. Interfaces* **2018,** *5*, 1800611.

(20) Guo, C.; Wei, S.; Zhou, S.; Zhang, T.; Wang, Z.; Ng, S. P.; Lu, X.; Wu, C. L.; Guo, W. Initial Reduction of CO_2 on Pd-, Ru-, and Cu-doped CeO_2 (111) Surfaces: Effects of Surface Modification on Catalytic Activity and Selectivity. *ACS Appl. Mater. Interfaces* **2017,** *9*, 26107-26117.

(21) Baran, T.; Wojtyła, S.; Dibenedetto, A.; Aresta, M.; Macyk, W. Zinc Sulfide Functionalized with Ruthenium Nanoparticles for Photocatalytic Reduction of CO_2. *Appl. Catal. B Environ.* **2015,** *178*, 170-176.

(22) Lee, G.-J.; Anandan, S.; Masten, S. J.; Wu, J. J. Photocatalytic Hydrogen Evolution from Water Splitting Using Cu Doped ZnS Microspheres under Visible Light Irradiation. *Renew.*

Energy **2016,** *89*, 18-26.

(23) Nasution, H.; Purnama, E.; Kosela, S.; Gunlazuardi, J. Photocatalytic Reduction of CO_2 on Copper-Doped Titania Catalysts Prepared by Improved-Impregnation Method. *Catal. Commun.* **2005,** *6*, 313-319.

(24) Pham, T.-D.; Lee, B.-K. Novel Photocatalytic Activity of Cu@V co-Doped TiO_2/PU for CO_2 Reduction with H_2O Vapor to Produce Solar Fuels under Visible Light. *J. Catal.* **2017,** *345*, 87-95.

(25) Hutter, J.; Iannuzzi, M.; Schiffmann, F.; VandeVondele, J. Cp2k: Atomistic Simulations of Condensed Matter Systems. *Wiley Interdiscip. Rev.: Comput. Mol. Sci.* **2014,** *4*, 15-25.

(26) Perdew, J. P.; Burke, K.; Ernzerhof, M. Generalized Gradient Approximation Made Simple. *Phys. Rev. Lett.* **1996,** *77*, 3865-3868.

(27) Grimme, S. Semiempirical GGA-type Density Functional Constructed with a Long-Range Dispersion Correction. *J. Comput. Chem.* **2006,** *27*, 1787-1799.

(28) VandeVondele, J.; Hutter, J. Gaussian Basis Sets for Accurate Calculations on Molecular Systems in Gas and Condensed Phases. *J. Chem. Phys.* **2007,** *127*, 114105.

(29) VandeVondele, J.; Krack, M.; Mohamed, F.; Parrinello, M.; Chassaing, T.; Hutter, J. Quickstep: Fast and Accurate Density Functional Calculations Using a Mixed Gaussian and Plane Waves Approach. *Comput. Phys. Commun.* **2005,** *167*, 103-128.

(30) Goedecker, S.; Teter, M.; Hutter, J. Separable Dual-Space Gaussian Pseudopotentials. *Phys. Rev. B* **1996,** *54*, 1703.

(31) Hartwigsen, C.; Gœdecker, S.; Hutter, J. Relativistic Separable Dual-Space Gaussian Pseudopotentials from H to Rn. *Phys. Rev. B* **1998,** *58*, 3641-3662.

(32) Ummartyotin, S.; Bunnak, N.; Juntaro, J.; Sain, M.; Manuspiya, H. Synthesis and Luminescence Properties of ZnS and Metal (Mn, Cu)-Doped-ZnS Ceramic Powder. *Solid State Sci.* **2012,** *14*, 299-304.

(33) Jiaguo Yu; Jun Zhang; Liu, S. Ion-Exchange Synthesis and Enhanced Visible-Light Photoactivity of CuS/ZnS Nanocomposite Hollow Spheres. *J. Phys. Chem. C* **2010,** *114*, 13642–13649.

(34) Li, N.; Zhang, L.; Zhou, J.; Jing, D.; Sun, Y. Localized Nano-Solid-Solution Induced by Cu Doping in ZnS for Efficient Solar Hydrogen Generation. *Dalton Trans.* **2014,** *43*, 11533-

11541.

(35) Ul Abideen, Z.; Teng, F. Enhanced Photochemical Activity and Stability of ZnS by a Simple Alkaline Treatment Approach. *CrystEngComm* **2018,** *20*, 7866-7879.

(36) Godefroo, S.; Hayne, M.; Jivanescu, M.; Stesmans, A.; Zacharias, M.; Lebedev, O. I.; Van Tendeloo, G.; Moshchalkov, V. V. Classification and Control of the Origin of Photoluminescence from Si Nanocrystals. *Nat. Nanotechnol.* **2008,** *3*, 174-178.

(37) Patel, S. P.; Pivin, J. C.; Chandra, R.; Kanjilal, D.; Kumar, L. Intrinsic Defects and Structural Phase of ZnS Nanocrystalline Thin Films: Effects of Substrate Temperature. *J. Mater. Sci.: Mater. Electron.* **2016,** *27*, 5640-5645.

(38) Arai, T.; Senda, S.-i.; Sato, Y.; Takahashi, H.; Shinoda, K.; Jeyadevan, B.; Tohji, K. Cu-Doped ZnS Hollow Particle with High Activity for Hydrogen Generation from Alkaline Dulfide Dolution under Visible Light. *Chem. Mater.* **2008,** *20*, 1997-2000.

(39) Zhu, X.; Ji, H.; Yi, J.; Yang, J.; She, X.; Ding, P.; Li, L.; Deng, J.; Qian, J.; Xu, H.; Li, H. A Specifically Exposed Cobalt Oxide/Carbon Nitride 2D Heterostructure for Carbon Dioxide Photoreduction. *Ind. Eng. Chem. Res.* **2018,** *57*, 17394-17400.

(40) Lin, L.; Li, H.; Yan, C.; Li, H.; Si, R.; Li, M.; Xiao, J.; Wang, G.; Bao, X. Synergistic Catalysis over Iron-Nitrogen Sites Anchored with Cobalt Phthalocyanine for Efficient CO_2 Electroreduction. *Adv. Mater.* **2019,** *31*, 1903470.

(41) Hammer, B.; Morikawa, Y.; Norskov, J. K. CO Chemisorption at Metal Surfaces and Overlayers. *Phys. Rev. Lett.* **1996,** *76*, 2141-2144.

Table of contents